Substrate-bound and substrate-free outward-facing structures of a multidrug ABC exporter

Vincent Chaptal, Veronica Zampieri, Benjamin Wiseman, Cédric Orelle, Juliette Martin, Kim-Anh Nguyen, Alexia Gobet, Margot Di Cesare, Sandrine Magnard, Waqas Javed, et al.

BIOCHEMISTRY

Substrate-bound and substrate-free outward-facing structures of a multidrug ABC exporter

Vincent Chaptal[1]†, Veronica Zampieri[1]†‡, Benjamin Wiseman[1,2]†§, Cédric Orelle[3]||, Juliette Martin[4]||, Kim-Anh Nguyen[5]||, Alexia Gobet[1]||, Margot Di Cesare[3]||, Sandrine Magnard[1], Waqas Javed[3]¶, Jad Eid[1], Arnaud Kilburg[1], Marine Peuchmaur[6], Julien Marcoux[7], Luca Monticelli[4], Martin Hogbom[2], Guy Schoehn[8], Jean-Michel Jault[3]#, Ahcène Boumendjel[5]#, Pierre Falson[1]*

Multidrug ABC transporters translocate drugs across membranes by a mechanism for which the molecular features of drug release are so far unknown. Here, we resolved three ATP-Mg^{2+}–bound outward-facing conformations of the *Bacillus subtilis* (homodimeric) BmrA by x-ray crystallography and single-particle cryo–electron microscopy (EM) in detergent solution, one of them with rhodamine 6G (R6G), a substrate exported by BmrA when overexpressed in *B. subtilis*. Two R6G molecules bind to the drug-binding cavity at the level of the outer leaflet, between transmembrane (TM) helices 1–2 of one monomer and TM5′–6′ of the other. They induce a rearrangement of TM1–2, highlighting a local flexibility that we confirmed by hydrogen/deuterium exchange and molecular dynamics simulations. In the absence of R6G, simulations show a fast postrelease occlusion of the cavity driven by hydrophobicity, while when present, R6G can move within the cavity, maintaining it open.

INTRODUCTION

Multidrug ATP-binding cassette (ABC) exporters transport a large panel of drugs conferring a multidrug resistance (MDR) cell phenotype that leads to chemotherapy failures against pathogenic microbes and cancers. Early conceptualized (*1*) ABC exporters mainly switch between a high drug affinity inward-facing (IF) conformation in which the drug-binding pocket in the membrane domain is exposed to the inner membrane leaflet, and a low drug affinity outward-facing (OF) conformation, favoring drug release outside the cells. These proteins are made of two transmembrane domains (TMDs) typically built with 12 transmembrane helices and two nucleotide-binding domains (NBDs). Drugs bind to the TMD, accessible from the inner membrane leaflet in the IF conformation. Two ATP molecules bind at the interface between the two NBDs (*2*, *3*), thereby stabilizing the dimer and favoring the drug occlusion that leads the reorganization of the TMD in an OF conformation (*4*).

Several exporter structures have been obtained (*5*–*13*), complemented with biochemical and biophysical characterizations [e.g., (*14*–*16*)], together contributing to a mechanistic understanding of the IF-to-OF transition. Moreover, the molecular mechanism by which structurally divergent drugs and compounds bind to the IF conformation is presently better understood, thanks to the structure of the human ABCB1 in complex with the anticancer drug taxol (*14*). This structure revealed that the substrate recognition is driven by the intrinsic plasticity of TM4 and TM10, required to accommodate the structure of the drug.

The question remains open as to how the structural variability of those substrates is handled by MDR ABC exporters to expel them and which molecular features of the protein in the OF conformation are driving this release step (*17*). So far, since the first structure released in 2006 (*5*) and almost 50 years after their discovery (*18*), no OF structure of an MDR ABC exporter with a bound substrate has been solved. To that aim, the ATP-bound cryo-EM structure of ABCC1 in the presence of its substrate, leukotriene C4, was resolved, but the location of the substrate was not determined (*19*). Previously, the crystal structure of the antibacterial peptide transporter McjD was obtained in complex with adenylyl-imidodiphosphate (AMP-PNP), and two molecules of nonyl-glucoside that were used as crystallization additive were bound in the putative drug-binding cavity (*8*). Molecular dynamics simulation based on that structure predicted a marked flexibility of the TM1–2 region (*20*), pointing to a possible role of this region in the release of substrates. However, so far, structural information is lacking to corroborate this hypothesis, mainly because of the poor affinity of the transported substrate in the OF conformation.

Here, we tackled the question by resolving three OF conformations of BmrA, a type IV ABC transporter (*21*, *22*) from *Bacillus subtilis* (*23*) conferring resistance to cervimycin C, an antibiotic produced by *Streptomyces tandæ* against gram-positive bacteria (*24*). Using an ATPase inactive mutant, E504A (*25*), we resolved its x-ray structure in complex with ATP-Mg^{2+}, which required several key steps optimization and to design specific stabilizers. We also resolved its cryo–electron microscopy (cryo-EM) structure in complex with

[1]Drug Resistance and Membrane Proteins Group, Molecular Microbiology and Structural Biochemistry Laboratory, CNRS UMR 5086, University of Lyon, IBCP, 7, passage du Vercors, 69367 Lyon, France. [2]Department of Biochemistry and Biophysics, Arrhenius Laboratories for Natural Sciences, Stockholm University, Stockholm, Sweden. [3]Bacterial Nucleotide-Binding Proteins Group, Molecular Microbiology and Structural Biochemistry Laboratory, CNRS UMR 5086, University of Lyon, IBCP, 7, passage du Vercors, 69367 Lyon, France. [4]Modeling Biological Macromolecules Group, Molecular Microbiology and Structural Biochemistry Laboratory, CNRS UMR 5086, University of Lyon, IBCP, 7, passage du Vercors, 69367 Lyon, France. [5]University of Grenoble Alpes, INSERM, LRB, 38000 Grenoble, France. [6]University of Grenoble Alpes, CNRS, DPM UMR 5063, 38041 Grenoble, France. [7]Institut de Pharmacologie et de Biologie Structurale (IPBS), UMR 5089, Université de Toulouse, CNRS, UPS, 31000 Toulouse, France. [8]University of Grenoble Alpes, CEA, CNRS, IBS, F-38000 Grenoble, France.
*Corresponding author. Email: pierre.falson@univ-lyon1.fr
†These authors contributed equally to this work as co-first authors.
‡Present address: European Molecular Biology Laboratory, 71 Avenue des Martyrs, CS 90181, 38042, Grenoble, Cedex 9, France.
§Present address: Department of Biosciences and Nutrition, Karolinska Institutet, Huddinge, Sweden.
||These authors contributed to this work as co-second authors.
¶Present address: University of Grenoble Alpes, CEA, CNRS, IBS, F-38000 Grenoble, France.
#These authors contributed to this work as co-penultimate authors.

ATP-Mg^{2+} and rhodamine 6G, a lipophilic cationic substrate of exporters, either from the ABC superfamily such as LmrA, a close homolog of BmrA (*26*), Cdr1 (*27*), Pdr5 (*28*) in yeast, and *Cyanidioschyzon merolæ* ABCB1 (*15*), or from Bmr and Blt, two other MDR transporters of *B. subtilis* (*29*), and AcrB of the resistance nodulation cell division (*30*). Comparison of the present structures enlightens how the drug binds before its release and shows how the flexibility of the TM1–2 segment drives this process, and this was confirmed by H/D exchange coupled to mass spectrometry (HDX-MS) and molecular dynamics simulations.

RESULTS

Crystal structure of BmrA in OF conformation in complex with ATP-Mg^{2+}

We first stabilized BmrA in its OF conformation by introducing the E504A mutation that prevents hydrolysis of ATP (*25*, *31*) and doxorubicin transport (fig. S1). The protein crystallized following the procedure setup for the mouse P-glycoprotein, using Triton X-100 for extraction and a mixture of *N*-dodecyl-β-D-*n*-maltopyranoside (DDM) and cholate for purification (*32*), which maintains a high ATPase activity level compared to DDM alone (fig. S1B). Quantification of detergents bound to BmrA (*33*) was helpful to produce high-quality crystals, as increasing cholate reduced the amount of DDM bound to BmrA up to 50%, which proportionally reduced the estimated detergent-belt size (Fig. 1A). Diffraction patterns of the resulting crystals displayed a lattice-doubling problem that prevented their processing and which we overcame by designing a series of tailored amphiphiles **3a**-**e** (Fig. 1B) with a scaffold based on glycosyl-substituted dicarboxylates surfactants (*34*). Of note, these additives increase the thermal stability of BmrA up to ~30°C for **3d** (Fig. 1C and data file S2), which helped produce better diffracting protein crystals (Fig. 1, D and E).

We reached 3.9-Å resolution for the BmrA E504A-ATP-Mg^{2+} complex in detergent solution (Fig. 2, left; figs. S2 and S3; and table S1). Even if the overall 3.9-Å resolution of this x-ray structure is modest, the quality of the phases from the model yielded very good maps for this resolution. Two dimers of BmrA were found in the asymmetric unit, with a root mean square deviation (RMSD) of 0.7 Å over 525 residues (fig. S2). Electron densities of each transmembrane helix were good enough to position them unambiguously (fig. S3A). It was also the same for TM1 and its following loop, pointed in this study, observed in each monomer (fig. S3B). The structure displays the characteristic type IV fold of ABC transporters (*21*), in which the NBDs bind two ATP-Mg^{2+} in a head-to-tail mode, capturing the BmrA-E504A mutant in complex with ATP-Mg^{2+} in a typical OF conformation. The E504A mutation stabilizes the efflux pump in an OF prehydrolytic state, similar to the one displayed by the wild-type (WT) BmrA trapped in the transition state for ATP hydrolysis in the presence of vanadate (*35*). The extracellular side of BmrA displays an opening to a cavity likely corresponding to the drug-exit path. In the context of this study, the crystal structure shows that some residues of the loop connecting TM1 to TM2 make contacts between half of the monomers of chains B and C (fig. S2, C and D) and another moiety of another dimer, while the other half remains free of movement (chains A and D). This suggests that these contacts are not required for maintaining the conformation of TM1–2 and/or modify the structure. For all structures, TM1 and TM2 are visible (fig. S3B), and the electron density for the loop in between is continuous for chains C and D. For chains A and B, small linkers between the TM and the middle of the loop are missing, denoting some intrinsic flexibility, but nevertheless still present and observable

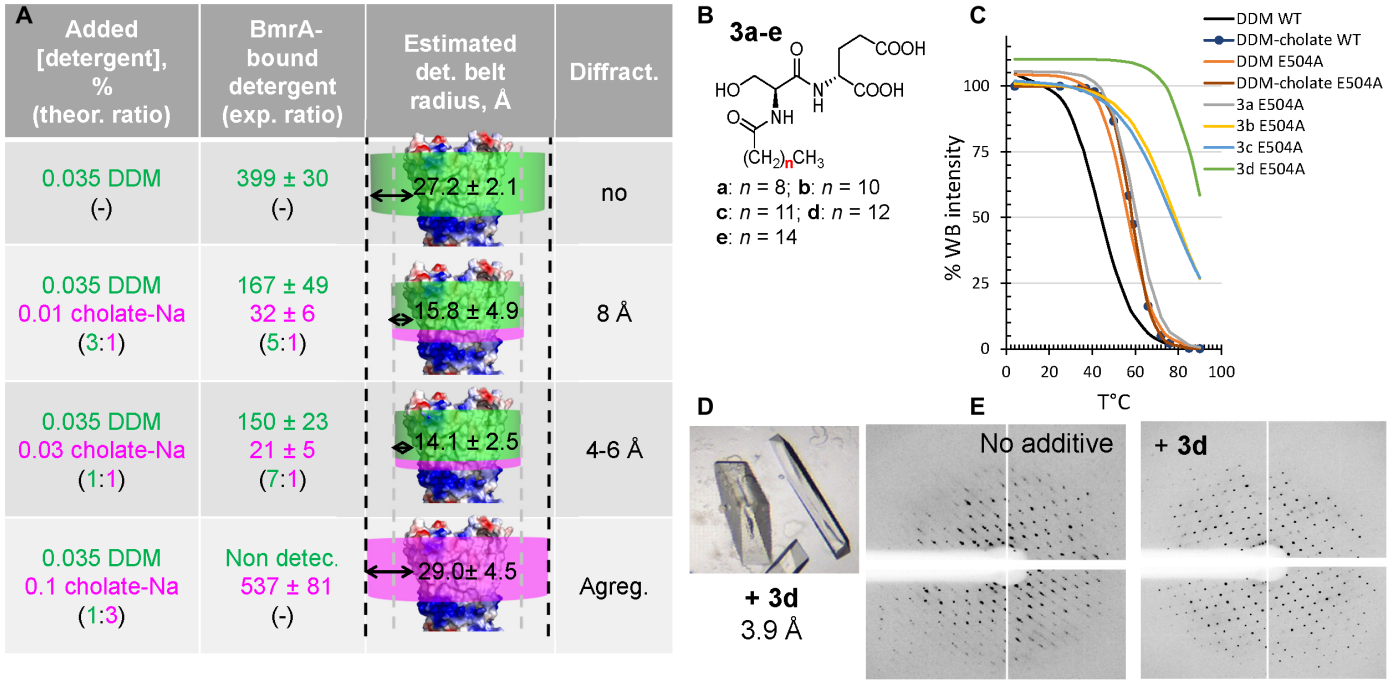

Fig. 1. Crystallization of BmrA in detergent solution. (**A**) Quantification of detergents bound to BmrA. See Materials and Methods and data file S1 for details. (**B**) Structure of the thermostabilizing amphiphilic additives. (**C**) Thermostabilization of BmrA. For clarity, fits (two to three independent assays) are displayed, with circles for the reference condition (DDM + cholate). Full data are provided in data file S2. (**D**) BmrA crystals in the presence of **3d**. (**E**) Lattice problem resolution with **3d**.

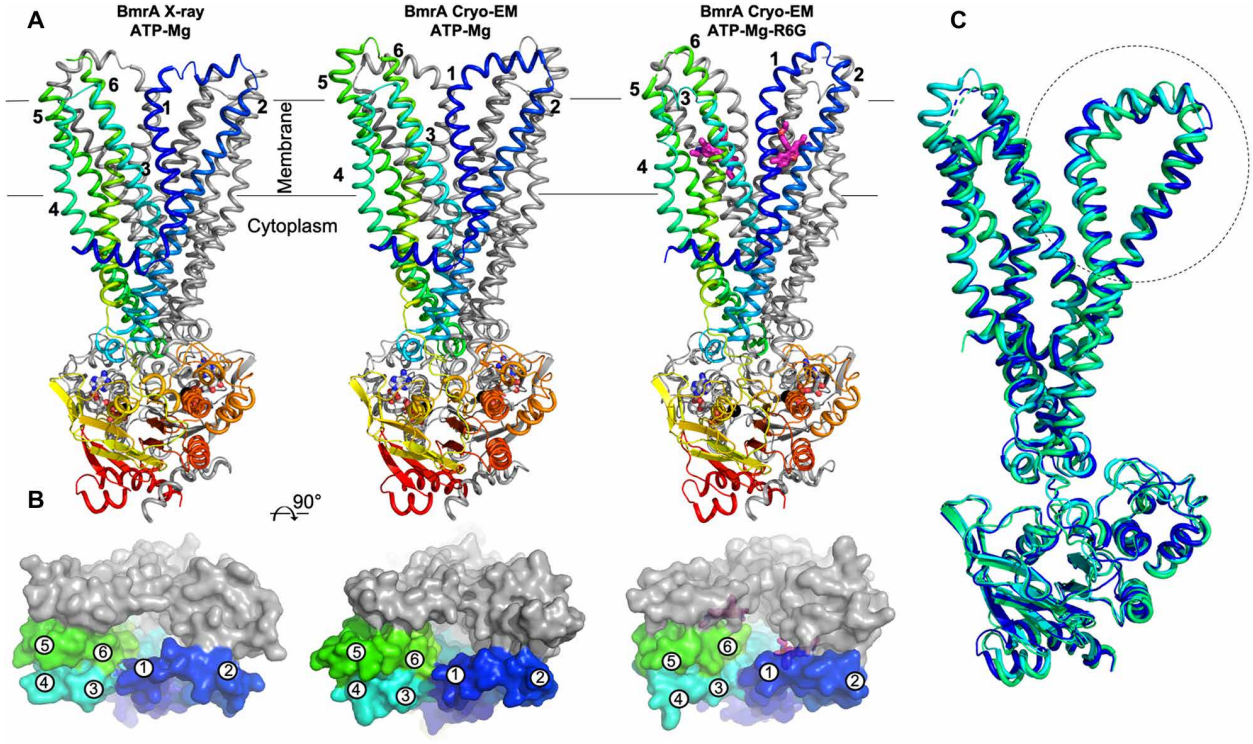

Fig. 2. X-ray and cryo-EM structures of the BmrA E504A mutant in complex with ATP-Mg^{2+} and R6G in detergent solution. (**A**) Cartoons of the transporter normal to the plane of the membrane. One monomer is in gray, and the other one is rainbow colored. TM helices are numbered for the colored monomer. ATP and R6G are displayed as sticks colored by atom type and Mg^{2+} as black sphere. (**B**) Surface representation of BmrA viewed from the extracellular side to highlight the difference in the OF cavity. (**C**) Superposition of the x-ray BmrA E504A [ATP-Mg^{2+}] (blue), cryo-EM BmrA E504A [ATP-Mg^{2+}] (cyan), and cryo-EM BmrA E504A [ATP-Mg^{2+}, R6G] (green).

when map contour is decreased. All the TM1–2 loops distribute around similar positions showing both the correctness of this position and the flexibility of this region (fig. S2E).

Cryo-EM structure of BmrA in the OF conformation in complex with R6G and ATP-Mg^{2+} in detergent solution

Incubating BmrA with known ligands (*23*) gave the best crystals with R6G. We could, however, not optimize them beyond 5 Å (fig. S4), leading us to move to single-particle cryo-EM (Fig. 2 and figs. S5 to S7). This approach allowed building the structure using the highest-resolution map using a C2 symmetry. Refinement up to 3.9 Å was carried out using both sharpened and unsharpened maps. Notably, the unsharpened map allowed observing the density corresponding to the TM1–2 loop (fig. S6). The resulting fold is very similar to that of the crystal structure with the difference in conformation of the region TM1–2 where TM1 is shifted toward TM2, resulting in a more pronounced opening of the cavity (Fig. 2B and table S2).

We observed two densities in the cryo-EM density map (Fig. 3A, bottom, and fig. S7CD), seen more clearly without the application of symmetry, and not present in the x-ray structure in which R6G was not added (Fig. 3A, top). To confirm this observation, we resolved by cryo-EM the structure of BmrA E504A in the same state, i.e., with ATP-Mg^{2+} and without R6G (Fig. 2, center, and figs. S8 to S10). The resolution increased to 3.6 Å with a map of better quality, allowing to build a full model of BmrA including notably the TM5–6 loop, which was not resolved before. The x-ray and cryo-EM structures are similar, with 1.06-Å RMSD over 573 residues, especially at the level of the TM1–2 region (Fig. 2C and fig. S11). Last, as for the x-ray structure, no additional density could be observed in the cryo-EM structure at the level of those observed in the central cavity of BmrA in the presence of R6G (Fig. 3A, middle).

Given the limited resolution, R6G, cholate, or the polar head of DDM could be positioned in these densities. We therefore carried out a series of biochemical assays with the WT and E504A mutant to discriminate between these possible ligands. Both proteins were purified in DDM or DDM-cholate, followed by a reconstitution into nanodiscs (*36*), on which we probed the binding of the three compounds. When purified in DDM-cholate, BmrA E504A binds R6G with a modest affinity of ~13 μM but is two times better in the presence of ATP-Mg^{2+} (Fig. 3C). The reverse effect was also observed, that is, ATP-Mg^{2+} binding with a twofold higher affinity when R6G is added (Fig. 3C). When purified in DDM, both WT and mutant BmrA displayed a similar better affinity for R6G (4.8 ± 0.9 and 3.3 ± 0.7 μM, $P < 0.0001$), while no specific interaction could be detected with cholate (fig. S12A) or DDM (or decyl maltoside at higher concentrations) when carrying the binding experiments with BmrA reconstituted into nanodiscs (fig. S12B). In contrast, R6G binds to the BmrA-nanodisc complexes with affinities as high as ~0.07 ± 0.09 μM ($P = 0.4$) and ~0.03 ± 0.02 μM ($P = 0.1$) for WT and mutant, respectively. Of note, R6G binds to nanodiscs themselves with an affinity of 3 to 7 μM (fig. S12, C and D). These results indicate that cholate and DDM do not bind to the drug-binding site of BmrA in contrast to R6G affinity that seems to be partially attenuated in that case by the ATP. Together, this led us to assume that this density reveals the occupancy of R6G, as displayed in Figs. 2 and 3 (A and B) and fig. S7 (C and D).

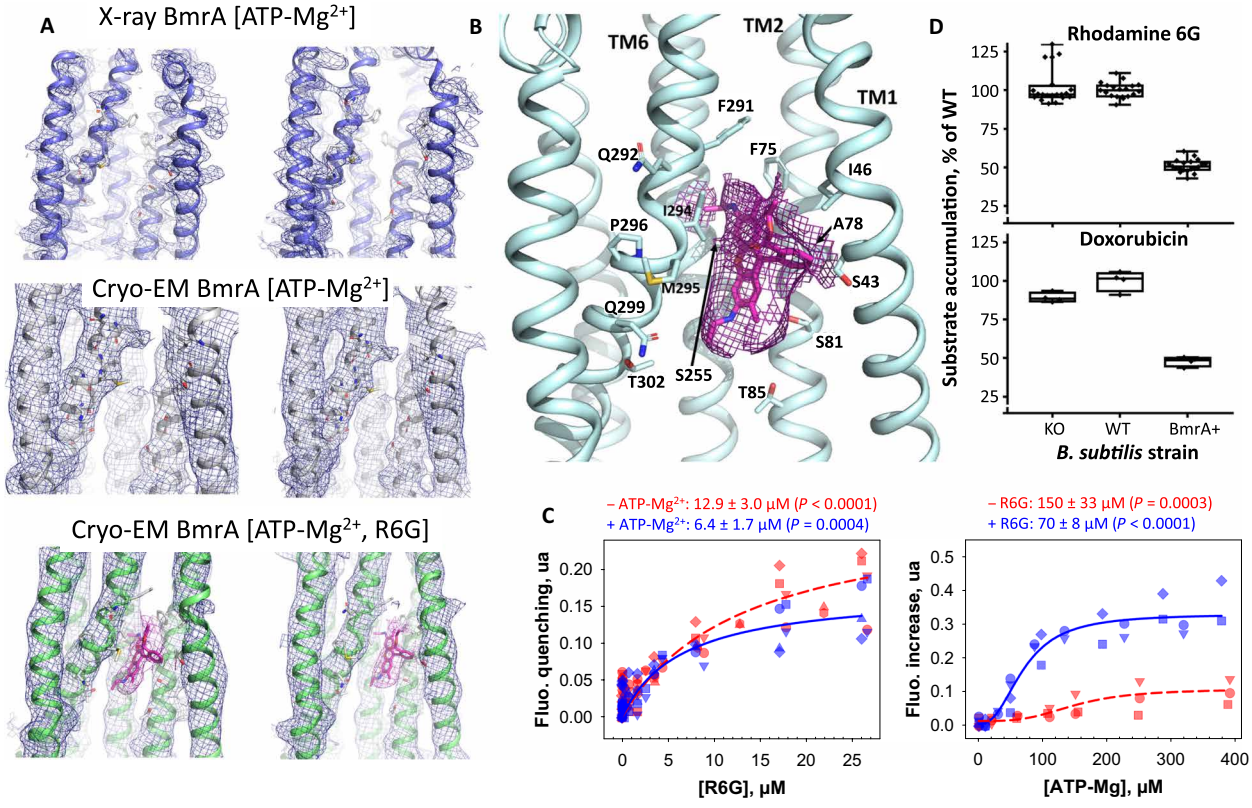

Fig. 3. R6G in the cryo-EM structure of BmrA E504A, efflux, and binding. (**A**) Superposition of the x-ray and cryo-EM structures and zoom in the two R6G regions. The x-ray map (2mFo-DFc) is displayed at 1σ and 0.8σ (EM BmrA E504A [ATP-Mg^{2+}] map) for the loop between TM1 and TM2. R6G structure and density are in magenta. (**B**) Detail of one R6G-binding site. (**C**) Binding of R6G (left) and ATP-Mg^{2+} (right) to BmrA E504A in DDM-cholate probed by intrinsic fluorescence, in the presence (blue) or absence (red) of 5 mM ATP-Mg^{2+} or 100 µM R6G, respectively. Symbols correspond to three to four independent experiments, fitted with equations S1 for R6G and S2 for ATP-Mg^{2+}. (**D**) R6G and doxorubicin accumulations in *B. subtilis* strains 168 ("WT"), KO for the gene coding for BmrA ("KO"), and 8R, a mutant of *B. subtilis* 168 strain overexpressing BmrA ("BmrA+"). Cells incubated with 5 µM substrate for 30 min at 37°C were then washed, lysed, and their intracellular fluorescence measured on supernatants, taking as reference the WT strain. Data are the average of 3 independent 3 to 10 replicates ($P < 10^{-10}$).

The observation above that R6G binding is enhanced by ATP-Mg^{2+}, even modestly, prompted us to investigate the possibility that BmrA could import R6G, since so far this molecule was only reported as a ligand of the pump (*23*). We therefore compared the intracellular accumulations of R6G and doxorubicin in three strains of *B. subtilis* previously described (*24*), either WT, invalidated for BmrA, or overexpressing BmrA (WT, KO, and BmrA+, respectively; Fig. 3D). While WT and KO strains display the same trends, the BmrA+ strain accumulates ~50% less each compound, therefore supporting the fact that R6G is a substrate of BmrA, which works as an exporter. Last, we also look at the stimulation of the ATPase activity of BmrA by the addition of substrates, but we could not detect any substantial effect of R6G, doxorubicin, or even Hoechst 33342 (fig. S12E), probably because of its high basal ATPase activity, as previously reported for this protein (*23*), and also for Cdr1 (*37*) and Pdr5 (*28*).

Two R6G molecules could be fitted in each density, although not in a perfect symmetrical position (Fig. 3A and fig. S7, C to F), explaining why the C2 symmetry does not improve those densities. R6G binds at the level of the outward leaflet, between TM1–2 of one monomer and TM5′–6′ of the other one. Each molecule is maintained in a hydrophobic cavity by a movement of TM1 toward TM2, mainly stabilized by van der Walls contacts with lateral chains of residues T39, S43, I46, F75, A78, I254′, S255′, L258′, F291′, I294′, and M295′. Few polar groups contribute also to the binding site including the alcohol group of S81, S225′, and T302′ and the carbonyl groups of A78, G251′, and F291′ (Fig. 3B and fig. S7, E and F). Such organization of the R6G pockets is close to that previously found in AcrB, together with the conformation of the R6G molecules themselves (fig. S7G). Several of these residues correspond to those found in the taxol-binding pocket of human ABCB1 in IF conformation (fig. S13) (*14*).

Structural differences between the structures of BmrA with and without substrate highlight the mobility of the TM1–2 region

Although quite similar, these structures of BmrA display important local differences rendering the substrate-exit path substantially different between them (Fig. 2). The differences originate from a displacement of the TM1–2 region, in the proximity of a kink starting in TM1 at residue P47 toward the end of TM1. Such displacement allows the central part of TM1 to shift from TM3 in the x-ray/cryo-EM structure toward TM2 in the cryo-EM + R6G structure. These differences between structures solved under identical or nearly identical conditions highlight a major local plasticity at the level of TM1–2. To evaluate its structural relevance, we tentatively

compared these structures with a panel of nucleotide-bound exporters of the same subtype IV: *Escherichia coli* McjD (*8*, *11*), *Thermus thermophilus* TmrAB (*13*), human (*4*) and *C. merolæ* (*15*) ABCB1, *E. coli* MsbA (*16*), *Staphylococcus aureus* Sav1866 (*5*), and *Thermotoga maritima* TM287/288 (*38*). Although the structural disparity of these different proteins, positioning them from the most occluded to the widest open (Fig. 4, A and B), suggested that TM1 in the x-ray and cryo-EM structures of BmrA without R6G may be oriented similarly as in McjD, ABCB1, and MsbA, conversely, TM2 may be shifted toward the OF conformation typically observed as in Sav1866. The loop connecting TM1 and TM2 has unwound on each side, allowing and/or accompanying the movement of TM2. In the cryo-EM structure with R6G, a consecutive displacement of TM1 shifting toward TM2 is seen, with an unwinding that takes place downward on TM1. The most open structures of Sav1866 and TM287/288 show TM1 and TM2 segments close together and separated from those forming the TM3–6 core. This motion of TM1–2 is concomitant with a wide opening of the cavity and a physical separation of the two TM3–6 cores that behave as rigid bodies. The movement might be granted by the intrinsic flexibility of ABC transporters on their external side, as suggested by molecular dynamics simulations carried out with McjD (*20*) and hinted by the B factors displayed in Fig. 4A.

Aligning the TM1–2 regions of these transporters with respect to their topologically conserved regions encompassing TM3–6 core and NBD allows visualizing the various conformations adopted by TM1–2, suggesting a hand fan motion (Fig. 4B and shown and detailed in Fig. 5F). We therefore explored the level of accessibility of TM1–2 of BmrA E504A in detergent solution by HDX-MS experiments (Fig. 4, C and D). We first observed that the trapping of the OF conformation by adding ATP-Mg^{2+} to the mutant increases the accessibility of the TM1–2 region (Fig. 4C). Several transmembrane peptides display a significantly higher deuterium uptake when adopting the OF conformation, notably those localized in the

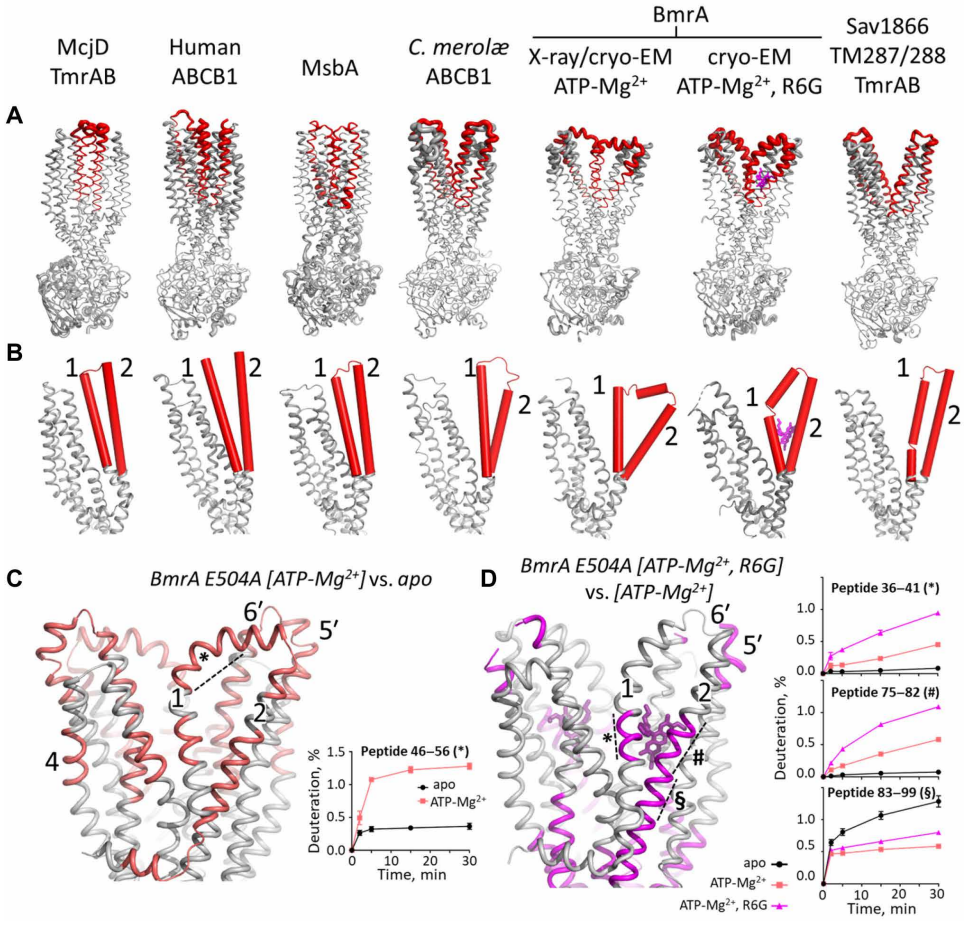

Fig. 4. Conformations and mobilities of TM1–2 in OF BmrA and other type IV ABC transporters. (**A**) Views (PDB codes) of McjD (**4pl0**, 5ofr), TmrAB (left: **6rai**, 6rak; right: 6rah-6raj), human (**6c0v**) and *C. merolæ* ABCB1 (**6a6m**), MsbA (**5ttp**), BmrA [this study, with ATP-Mg^{2+} (x-ray: 6r72; cryo-EM: **7ow8**) and with ATP-$Mg^{2+}$and R6G cryo-EM: **7bg4**), Sav1866 (**2hyd**), and TM287/288 (**6qv0**, 6qv1, 6qv2), superimposed from TM3 to TM6 and displayed from left to right from the most occluded to the widest open conformation. For clarity, only structures with bold PDB codes are displayed. Cartoon thickness is proportional to B factor. TM1–2 is colored in red. (**B**) Close-up view of TM1–6 of each monomer (and of the N-terminal half of ABCB1) with the TM1–2 segment in red cylinders. (**C** and **D**) HDX-MS experiments of BmrA E504A in DDM-cholate identifying the TM regions with increased deuterium accessibility in the OF state. (C) displays the ATP-Mg^{2+}-bound state as compared to the apo state. (D) compares the ATP-Mg^{2+}–bound state with and without R6G. Pictures display the accessible regions after 30-min exchange, colored in salmon ($P < 0.01$) and magenta ($P < 0.001$). Time-dependent deuteration plots of the indicated peptides are shown.

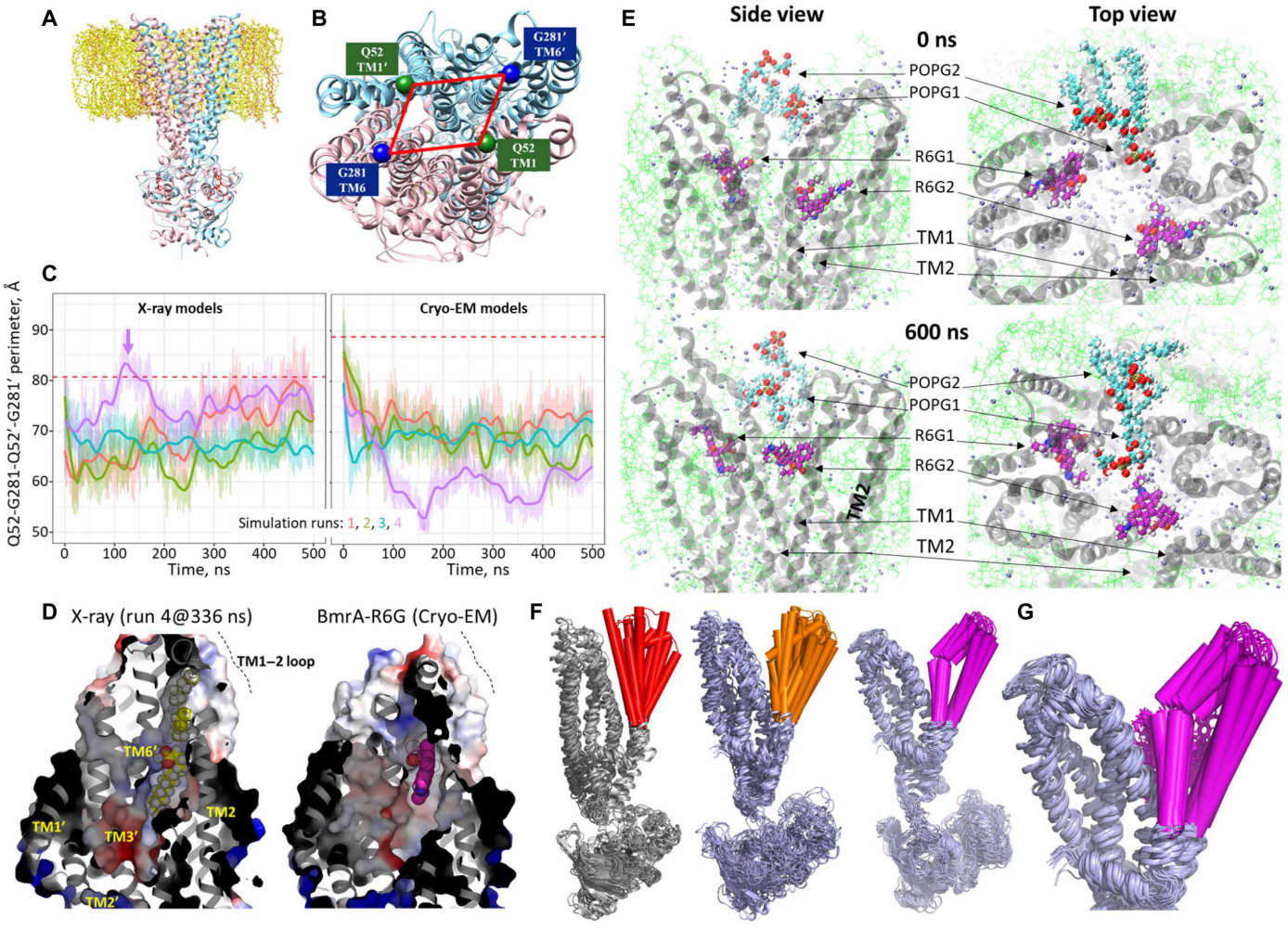

Fig. 5. Dynamics of the BmrA TMD region. (**A**) Starting model of BmrA in a lipid bilayer. Chains A and B are colored in pink and cyan, ATP in red, and lipids in yellow. (**B**) Close-up view showing residues chosen for measuring the perimeter of the cavity. (**C**) Time evolution of the cavity perimeter for each simulation. Red dashed lines indicate the initial values of the distances. The arrow indicates the time at which a POPG molecule inserts through TM1–2 in the fourth simulation. (**D**) Electrostatic maps of the BmrA, either from simulation 4 from the x-ray structure taken at 336 ns with the POPG binding to the substrate-binding pocket (left) and from the cryo-EM structure with R6G (right). (**E**) Snapshots of the molecular dynamics of BmrA E504A [ATP-Mg^{2+}, R6G] at 0 and 600 ns. Additional snapshots at 300 and 900 ns are displayed in fig. S19A. POPG molecules coming into the cavity are in cyan. (**F**) Superimposition of the structures displayed in Fig. 3A with TM1–2 in red and comparison with the poses got by molecular dynamic simulations carried out without (orange) and with (magenta) R6G (R6G molecules have been omitted for clarity. (**G**) Close-up view of the poses with R6G.

TM1–2 region such as the peptides 46 to 56 (asterisk in Fig. 4C). Such trend is also observed in nanodiscs and comparable to the WT BmrA stabilized by Vi trapping (fig. S14). Note that as compared to the detergent environment, in nanodiscs, a smaller number of transmembrane peptides show an increased deuteration, but they still mostly localize to TM1, TM2, and TM6. We then observed that the addition of R6G to BmrA E504A in complex with ATP-Mg^{2+} significantly increases the accessibility to deuterium of the main chain of transmembrane parts surrounding the R6G-binding region, notably peptides 36 to 41 and 75 to 82 in TM1 and TM2, respectively, translating a structural rearrangement consistent with a widener opening of TM1–2 in the presence of R6G (Fig. 4D). Together, these results are consistent with the mechanical plasticity of TM1–2 inferred from the x-ray and cryo-EM structures of BmrA, which may be a key feature of MDR pumps allowing the release of substrates varying in size and shape.

Molecular dynamics simulations of x-ray and cryo-EM structures of BmrA

To get a dynamic view of the substrate-exit site of BmrA, we performed two series of all-atom molecular dynamics simulations of BmrA in complex with ATP-Mg^{2+} reconstituted in a lipid bilayer (Fig. 5A), either without or with R6G.

First, we investigated dynamics of BmrA in the absence of R6G. We carried out four simulations of 500 ns on each x-ray and cryo-EM (+R6G from which we removed it) structures under identical conditions using different starting velocities. We estimated the size of the substrate-exit cavity by measuring the variation with time of the perimeter formed by the Cα of the two residues Q52 in TM1 and G281 in TM6 of each monomer (Fig. 5, B and C). As shown, the initial perimeter of the cryo-EM structure, up to 90 Å, was larger than that of the x-ray one, up to 80 Å. Considering the simulation settings and the limited resolution of the structures, we expected to

observe only changes driven by strong forces. All the models undergo a closure (Fig. 5C and fig. S15), reaching a common perimeter of ~70 Å. BmrA shifts toward the most occluded states, as the one observed in MsbA and ABCB1 in Fig. 4 (A and B). This closure is rapid, generally occurring within the initial 100 ns, as also proposed for the extracellular gate of TmrAB (*13*). It contrasts with the stabilized wider open conformation of the x-ray and cryo-EM experiments, possibly because of the DDM-cholate mixture in which BmrA is maintained in these experiments contrarily to the simulations. This fast closure is followed by large-scale structural fluctuations (fig. S16). Of note, a closure was also obtained in simulations with longer equilibration steps. An unexpected result came from the fourth simulation generated from the x-ray structure, which, by contrast to the others, rapidly opens during the first 100 ns its substrate-exit cavity up to ~83 Å (magenta trace in Fig. 5C, left). This movement enlarges enough the lateral opening between TM1 and TM2 to allow a POPG [2-oleoyl-1-palmitoyl-sn-glycero-3-phospho-rac-(1-glycerol)] molecule to penetrate through it and move to the substrate-binding cavity (Fig. 5D, left) in one R6G-binding site (Fig. 5D, right). One aliphatic chain of the lipid lays in the hydrophobic pocket, while its polar head is oriented toward the center of the cavity, as R6G.

Then, we carried out three simulations starting with the cryo-EM structure with R6G for 1 μs and using the same settings. We parameterized the R6G, starting from the molecule in the cryo-EM structure, and then optimized it in a membrane environment (R6G parameterization files rhodamine6G.itp and forcefieldR6G.itp; fig. S17). By contrast with the dynamics carried out above without R6G, in the present ones, BmrA remains open in the OF conformation, leading to a rather constant Q52-G281-Q52′-G281′ perimeter, which ranges between 95 and 115 Å (fig. S18A). One R6G (R6G2 in run 1) among the six of the three simulations substantially moved within the binding pocket (fig. S18B), going to the center of the cavity in ~300 ns and then coming back to its initial location (Fig. 5E and fig. S18C). The movement of this R6G is accompanied with more contacts with water (fig. S19A) and less with protein (fig. S19B), which is typical of a solvation step preceding the release. However, such release does not occur as, early in the simulations, two lipids invade the pocket above the R6G molecules, forming a cap preventing their release (POPG 1 and 2 in Fig. 5E and fig. S18C). Since it cannot be expelled through the center of the pocket, the R6G2 molecules go back to its original location near TM1–2 in ~400 ns, through which it also cannot be expelled because of the presence of lipids blocking this access (Fig. 5E). A longer simulation time would be necessary to allow a release of the substrate.

Last, we observed that the poses generated by the molecular dynamics of BmrA carried out in absence of R6G nicely reproduces the hand fan motion of TM1–2 introduced above as suggested by the superposition of the various type IV ABC structures displayed in Fig. 4A (Fig. 5F, left versus center). In presence of R6G, this hand fan movement is substantially reduced (Fig. 5F, right), with TM1–2 being stabilized by the substrate (Fig. 5G). Notably, for the half of the transporter where R6G moves away from the binding site, the transporter moves in concert accompanying R6G movement with plastic deformation of the binding site, highlighting adaptation of BmrA to its local substrate presence (fig. S19C).

DISCUSSION

The BmrA structures presented here unravel new conformations in the landscape of structures of multidrug ABC transporters resolved in OF conformations, and one of them reveals a structure of a type IV MDR ABC transporter with its transported substrate in a substrate-release competent state. The R6G molecules are located at the level of the outer leaflet and are poised to be released from the transporter. Several parameters have contributed to stabilize this ternary complex, among them the positive effect of R6G and ATP-Mg^{2+} on their mutual affinities, together with the amphipathic nature of R6G added of a marked hydrophobicity. The present structures reveal a substrate-release site made of flexible (TM1–2) and rigid (TM3–6) regions. Combined with HDX-MS and molecular dynamics simulations, they provide new information on the mechanism of substrate release from the substrate-binding pocket and suggest how the transporter may reset to an occluded conformation by closing back on itself immediately after substrate release. The flexibility of multidrug ABC transporters has been well established in IF states, sampling different conformations that facilitate recognition of multiple compounds (*35*, *39*, *40*). The current study reveals that such a flexibility is also sampled in OF conformations, presumably with a lower amplitude. We propose that this flexibility is required to adapt the site to various substrates' sizes, essential to secure their release to the extracellular side, and also to reset the transporter back to an occluded state, thereby preventing any trans-inhibition mechanism as reported recently (*41*). Such flexibility is also consistent with the fast dynamics of the extracellular gate of TM287/288 observed in EPR experiments (*42*) and suggests that no additional energy input is needed for substrate release.

A key point arises when comparing the fast closure revealed by the simulations with the stabilized outward states observed in both x-ray and cryo-EM structures. A similar flexibility of the external part of the transmembrane segments is observed in the structures and simulations. In the case of experimental structures, the hydrophobic nature of the substrate-binding cavity, together with the accessibility to water, may favor its filling with amphipathic detergents and stabilize this conformation, as seen previously by molecular dynamic simulations carried out on the OF conformation of Sav1866 in the presence of DDM (*33*). The fact that detergents are poor membrane mimetics and that the structures are those of a biochemically

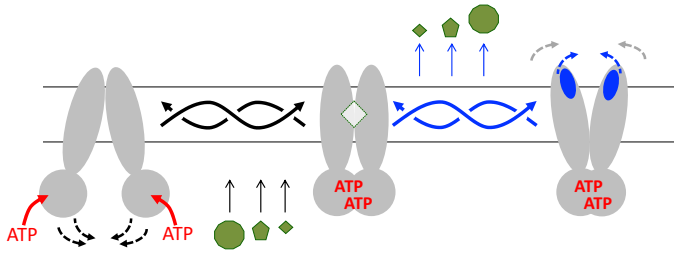

Fig. 6. Model of mechanism of efflux. Left: IF conformation of the transporter displaying flexibility at the NBD level, with different degrees of opening of the substrate-binding cavity (black dotted arrows) and allowing for diverse shapes and sizes of substrates. **Middle:** Occluded conformation. **Right:** OF substrate-release conformation. Release occurs via a plastic deformation of the external part of the transmembrane region. Deformation of the apex is adapted to the size or chemical property of the substrates (blue dotted arrows). Hydrophobicity of the substrate-binding pocket triggers the immediate closing of the external part of the transporter, which swings back to the occluded state. ATP hydrolysis occurs, followed by ADP and Pi release resulting in the opening in the IF conformation again, ready for another swing. Twisted arrows exemplify the different routes the transporter can take to reach any conformation, granted by the local deformability of the transmembrane helices.

stabilized version of BmrA (E504A) may have also contributed to stabilize this conformation. Although detergent molecules are too mobile and flexible to be observed at these resolutions, they do however constitute excellent tools to capture such transient states. In the case of simulations in lipid membrane, the hydrophobic pocket is exposed to water, which is extremely unfavorable and leads to a rapid motion of TM1–2 that closes the pocket to shield it from water. Molecular dynamics simulations carried out with McjD have predicted a marked flexibility of the TM1–2 region (*20*), later observed by single-molecule Förster resonance energy transfer (*43*), pointing to a possible role of this region in the release of substrates. This motion appears sufficient per se to reset the transporter back to an occluded conformation. The hydrophobicity of the substrate-binding pocket is so important that in one simulation, a lipid moved into the cavity (Fig. 5, C and D), causing the cavity to remain open. This result fits well with the presence of a detergent molecule in the binding pocket of McjD (*8*) together with the very recent discovery of a lipid inside the structure of the major facilitator superfamily protein LrmP (*44*).

Together, these data emphasize that independent of ATP hydrolysis, hydrophobicity of the substrate-binding pocket alone could promote pocket closure, following a mechanism that may be similar to the hydrophobic collapse described for ion-gated channels (*45*). The intrinsic flexibility of the IF and OF conformations, documented here and well characterized at the level of the NBDs and TMD (*39*, *43*, *46*, *47*), together with this hydrophobic collapse, leads us to favor a mechanism of transport as depicted in Fig. 6. As schematized, the intrinsic flexibility of the exporter in the IF state first allows it to sample multiple conformations adjusting for chemically unrelated substrates. Binding of ATP then leads to the occluded conformation that transiently traps the substrate, and then followed by a plastic deformation of the outward-most part of the exporter (e.g., exemplified with the cartoon thickness proportional to the B factor in Fig. 4A). Again, this plasticity allows the exporter first to accommodate the chemical variability of the substrates and second to release them. The hydrophobic collapse of the substrate-binding pocket then triggers the closing of the transporter, without additional energy input [leading to the hypothesis that ATP hydrolysis occurs after substrate release, as already proposed (*19*, *38*)], allowing the exporter to swing back toward the IF conformation, ready to take on a new molecule. Consequently, in this model, intrinsic plasticity and hydrophobicity collapse alleviate the need for precisely defined conformations at each stage of transport (symbolized by the twisted blue and black arrows in Fig. 6).

MATERIALS AND METHODS

Materials and Methods are detailed in the Supplementary Materials and Methods. BmrA expression and purification were adapted from methods previously reported (*23*, *48*). Thermostabilization assays were carried out as previously reported (*34*). DDM and cholate quantifications were done as described in (*33*) and (*49*), respectively. The ATPase activity of BmrA was measured as previously described (*34*). The MSP1E3D1 protein was expressed and purified and reconstituted with lipids and BmrA as previously described (*36*). Ligand binding, transport, accumulation, and HDX experiments are detailed in the Supplementary Materials and Methods. BmrA crystallization and additive syntheses, cryo-EM assays, and in silico simulations are detailed in the Supplementary Materials and Methods.

SUPPLEMENTARY MATERIALS

Supplementary material for this article is available at https://science.org/doi/10.1126/sciadv.abg9215

View/request a protocol for this paper from *Bio-protocol*.

REFERENCES AND NOTES

1. O. Jardetzky, Simple allosteric model for membrane pumps. *Nature* **211**, 969–970 (1966).
2. K. Linton, C. Higgins, Structure and function of ABC transporters: The ATP switch provides flexible control. *Pflügers Arch.* **453**, 555–567 (2007).
3. K. P. Locher, Mechanistic diversity in ATP-binding cassette (ABC) transporters. *Nat. Struct. Mol. Biol.* **23**, 487–493 (2016).
4. Y. Kim, J. Chen, Molecular structure of human P-glycoprotein in the ATP-bound, outward-facing conformation. *Science* **359**, 915–919 (2018).
5. R. J. Dawson, K. P. Locher, Structure of a bacterial multidrug ABC transporter. *Nature* **443**, 180–185 (2006).
6. A. Ward, C. L. Reyes, J. Yu, C. B. Roth, G. Chang, Flexibility in the ABC transporter MsbA: Alternating access with a twist. *Proc. Natl. Acad. Sci.* **104**, 19005–19010 (2007).
7. A. B. Ward, P. Szewczyk, V. Grimard, C. W. Lee, L. Martinez, R. Doshi, A. Caya, M. Villaluz, E. Pardon, C. Cregger, D. J. Swartz, P. G. Falson, I. L. Urbatsch, C. Govaerts, J. Steyaert, G. Chang, Structures of P-glycoprotein reveal its conformational flexibility and an epitope on the nucleotide-binding domain. *Proc. Natl. Acad. Sci. U.S.A.* **110**, 13386–13391 (2013).
8. H. G. Choudhury, Z. Tong, I. Mathavan, Y. Li, S. Iwata, S. Zirah, S. Rebuffat, H. W. van Veen, K. Beis, Structure of an antibacterial peptide ATP-binding cassette transporter in a novel outward occluded state. *Proc. Natl. Acad. Sci. U.S.A.* **111**, 9145–9150 (2014).
9. A. Blees, D. Januliene, T. Hofmann, N. Koller, C. Schmidt, S. Trowitzsch, A. Moeller, R. Tampé, Structure of the human MHC-I peptide-loading complex. *Nature* **551**, 525–528 (2017).
10. Z. L. Johnson, J. Chen, Structural basis of substrate recognition by the multidrug resistance protein MRP1. *Cell* **168**, 1075–1085.e9 (2017).
11. K. Bountra, G. Hagelueken, H. G. Choudhury, V. Corradi, K. el Omari, A. Wagner, I. Mathavan, S. Zirah, W. Yuan Wahlgren, D. P. Tieleman, O. Schiemann, S. Rebuffat, K. Beis, Structural basis for antibacterial peptide self-immunity by the bacterial ABC transporter McjD. *EMBO J.* **36**, 3062–3079 (2017).
12. H. Göddeke, M. H. Timachi, C. A. J. Hutter, L. Galazzo, M. A. Seeger, M. Karttunen, E. Bordignon, L. V. Schäfer, Atomistic mechanism of large-scale conformational transition in a heterodimeric ABC exporter. *J. Am. Chem. Soc.* **140**, 4543–4551 (2018).
13. S. Hofmann, D. Januliene, A. R. Mehdipour, C. Thomas, E. Stefan, S. Brüchert, B. T. Kuhn, E. R. Geertsma, G. Hummer, R. Tampé, A. Moeller, Conformation space of a heterodimeric ABC exporter under turnover conditions. *Nature* **571**, 580–583 (2019).
14. A. Alam, J. Kowal, E. Broude, I. Roninson, K. P. Locher, Structural insight into substrate and inhibitor discrimination by human P-glycoprotein. *Science* **363**, 753–756 (2019).
15. A. Kodan, T. Yamaguchi, T. Nakatsu, K. Matsuoka, Y. Kimura, K. Ueda, H. Kato, Inward- and outward-facing X-ray crystal structures of homodimeric P-glycoprotein CmABCB1. *Nat. Commun.* **10**, 88 (2019).
16. W. Mi, Y. Li, S. H. Yoon, R. K. Ernst, T. Walz, M. Liao, Structural basis of MsbA-mediated lipopolysaccharide transport. *Nature* **549**, 233–237 (2017).
17. O. Lewinson, C. Orelle, M. A. Seeger, Structures of ABC transporters: Handle with care. *FEBS Lett.* **594**, 3799–3814 (2020).
18. R. L. Juliano, V. Ling, A surface glycoprotein modulating drug permeability in Chinese hamster ovary cell mutants. *Biochim. Biophys. Acta* **455**, 152–162 (1976).
19. Z. L. Johnson, J. Chen, ATP binding enables substrate release from multidrug resistance protein 1. *Cell* **172**, 81–89.e10 (2018).
20. R. X. Gu, V. Corradi, G. Singh, H. G. Choudhury, K. Beis, D. P. Tieleman, Conformational changes of the antibacterial peptide ATP binding cassette transporter McjD revealed by molecular dynamics simulations. *Biochemistry* **54**, 5989–5998 (2015).
21. C. Thomas, R. Tampé, Structural and mechanistic principles of ABC transporters. *Annu. Rev. Biochem.* **89**, 605–636 (2020).
22. C. Thomas, S. G. Aller, K. Beis, E. P. Carpenter, G. Chang, L. Chen, E. Dassa, M. Dean, F. Duong van Hoa, D. Ekiert, R. Ford, R. Gaudet, X. Gong, I. B. Holland, Y. Huang, D. K. Kahne, H. Kato, V. Koronakis, C. M. Koth, Y. Lee, O. Lewinson, R. Lill, E. Martinoia, S. Murakami, H. W. Pinkett, B. Poolman, D. Rosenbaum, B. Sarkadi, L. Schmitt, E. Schneider, Y. Shi, S. L. Shyng, D. J. Slotboom, E. Tajkhorshid, D. P. Tieleman, K. Ueda, A. Váradi, P. C. Wen, N. Yan, P. Zhang, H. Zheng, J. Zimmer, R. Tampé, Structural and functional diversity calls for a new classification of ABC transporters. *FEBS Lett.* **594**, 3767–3775 (2020).
23. E. Steinfels, C. Orelle, J. R. Fantino, O. Dalmas, J. L. Rigaud, F. Denizot, A. di Pietro, J. M. Jault, Characterization of YvcC (BmrA), a multidrug ABC transporter constitutively expressed in *Bacillus subtilis*. *Biochemistry* **43**, 7491–7502 (2004).
24. H. Krügel, A. Licht, G. Biedermann, A. Petzold, J. Lassak, Y. Hupfer, B. Schlott, C. Hertweck, M. Platzer, S. Brantl, H. P. Saluz, Cervimycin C resistance in *Bacillus subtilis* is due to a promoter up-mutation and increased mRNA stability of the constitutive ABC-transporter gene bmrA. *FEMS Microbiol. Lett.* **313**, 155–163 (2010).

25. C. Orelle, O. Dalmas, P. Gros, A. Di Pietro, J. M. Jault, The conserved glutamate residue adjacent to the Walker-B motif is the catalytic base for ATP hydrolysis in the ATP-binding cassette transporter BmrA. *J. Biol. Chem.* **278**, 47002–47008 (2003).
26. H. W. van Veen, K. Venema, H. Bolhuis, I. Oussenko, J. Kok, B. Poolman, A. J. Driessen, W. N. Konings, Multidrug resistance mediated by a bacterial homolog of the human multidrug transporter MDR1. *Proc. Natl. Acad. Sci. U.S.A.* **93**, 10668–10672 (1996).
27. S. Nim, L. G. Lobato, A. Moreno, V. Chaptal, M. K. Rawal, P. Falson, R. Prasad, Atomic modelling and systematic mutagenesis identify residues in multiple drug binding sites that are essential for drug resistance in the major *Candida* transporter Cdr1. *Biochim. Biophys. Acta* **1858**, 2858–2870 (2016).
28. R. Ernst, P. Kueppers, C. M. Klein, T. Schwarzmueller, K. Kuchler, L. Schmitt, A mutation of the H-loop selectively affects rhodamine transport by the yeast multidrug ABC transporter Pdr5. *Proc. Natl. Acad. Sci. U.S.A.* **105**, 5069–5074 (2008).
29. M. Ahmed, L. Lyass, P. N. Markham, S. S. Taylor, N. Vázquez-Laslop, A. A. Neyfakh, Two highly similar multidrug transporters of *Bacillus subtilis* whose expression is differentially regulated. *J. Bacteriol.* **177**, 3904–3910 (1995).
30. H. Sjuts, A. V. Vargiu, S. M. Kwasny, S. T. Nguyen, H. S. Kim, X. Ding, A. R. Ornik, P. Ruggerone, T. L. Bowlin, H. Nikaido, K. M. Pos, T. J. Opperman, Molecular basis for inhibition of AcrB multidrug efflux pump by novel and powerful pyranopyridine derivatives. *Proc. Natl. Acad. Sci. U.S.A.* **113**, 3509–3514 (2016).
31. C. Orelle, F. Gubellini, A. Durand, S. Marco, D. Lévy, P. Gros, A. di Pietro, J. M. Jault, Conformational change induced by ATP binding in the multidrug ATP-binding cassette transporter BmrA. *Biochemistry* **47**, 2404–2412 (2008).
32. S. G. Aller, J. Yu, A. Ward, Y. Weng, S. Chittaboina, R. Zhuo, P. M. Harrell, Y. T. Trinh, Q. Zhang, I. L. Urbatsch, G. Chang, Structure of P-glycoprotein reveals a molecular basis for poly-specific drug binding. *Science* **323**, 1718–1722 (2009).
33. V. Chaptal, F. Delolme, A. Kilburg, S. Magnard, C. Montigny, M. Picard, C. Prier, L. Monticelli, O. Bornert, M. Agez, S. Ravaud, C. Orelle, R. Wagner, A. Jawhari, I. Broutin, E. Pebay-Peyroula, J. M. Jault, H. R. Kaback, M. le Maire, P. Falson, Quantification of detergents complexed with membrane proteins. *Sci. Rep.* **7**, 41751 (2017).
34. K. A. Nguyen, M. Peuchmaur, S. Magnard, R. Haudecoeur, C. Boyère, S. Mounien, I. Benammar, V. Zampieri, S. Igonet, V. Chaptal, A. Jawhari, A. Boumendjel, P. Falson, Glycosyl-substituted dicarboxylates as detergents for the extraction, overstabilization, and crystallization of membrane proteins. *Angew. Chem. Int. Ed. Engl.* **57**, 2948–2952 (2018).
35. D. Lacabanne, C. Orelle, L. Lecoq, B. Kunert, C. Chuilon, T. Wiegand, S. Ravaud, J. M. Jault, B. H. Meier, A. Böckmann, Flexible-to-rigid transition is central for substrate transport in the ABC transporter BmrA from *Bacillus subtilis*. *Commun. Biol.* **2**, 149 (2019).
36. F. J. Alvarez, C. Orelle, A. L. Davidson, Functional reconstitution of an ABC transporter in nanodiscs for use in electron paramagnetic resonance spectroscopy. *J. Am. Chem. Soc.* **132**, 9513–9515 (2010).
37. S. Shukla, V. Rai, D. Banerjee, R. Prasad, Characterization of Cdr1p, a major multidrug efflux protein of *Candida albicans*: Purified protein is amenable to intrinsic fluorescence analysis. *Biochemistry* **45**, 2425–2435 (2006).
38. C. A. J. Hutter, M. H. Timachi, L. M. Hürlimann, I. Zimmermann, P. Egloff, H. Göddeke, S. Kucher, S. Štefanić, M. Karttunen, L. V. Schäfer, E. Bordignon, M. A. Seeger, The extracellular gate shapes the energy profile of an ABC exporter. *Nat. Commun.* **10**, 2260 (2019).
39. S. Mehmood, C. Domene, E. Forest, J. M. Jault, Dynamics of a bacterial multidrug ABC transporter in the inward- and outward-facing conformations. *Proc. Natl. Acad. Sci. U.S.A.* **109**, 10832–10836 (2012).
40. P. C. Wen, B. Verhalen, S. Wilkens, H. S. McHaourab, E. Tajkhorshid, On the origin of large flexibility of P-glycoprotein in the inward-facing state. *J. Biol. Chem.* **288**, 19211–19220 (2013).
41. K. Barth, S. Hank, P. E. Spindler, T. F. Prisner, R. Tampé, B. Joseph, Conformational coupling and trans-inhibition in the human antigen transporter ortholog TmrAB resolved with dipolar EPR spectroscopy. *J. Am. Chem. Soc.* **140**, 4527–4533 (2018).
42. M. H. Timachi, C. A. J. Hutter, M. Hohl, T. Assafa, S. Böhm, A. Mittal, M. A. Seeger, E. Bordignon, Exploring conformational equilibria of a heterodimeric ABC transporter. *eLife* **6**, e20236 (2017).
43. F. Husada, K. Bountra, K. Tassis, M. Boer, M. Romano, S. Rebuffat, K. Beis, T. Cordes, Conformational dynamics of the ABC transporter McjD seen by single-molecule FRET. *EMBO J.* **37**, e100056 (2018).
44. V. Debruycker, A. Hutchin, M. Masureel, E. Ficici, C. Martens, P. Legrand, R. A. Stein, H. S. Mchaourab, J. D. Faraldo-Gómez, H. Remaut, C. Govaerts, An embedded lipid in the multidrug transporter LmrP suggests a mechanism for polyspecificity. *Nat. Struct. Mol. Biol.* **27**, 829–835 (2020).
45. M. O. Jensen, D. W. Borhani, K. Lindorff-Larsen, P. Maragakis, V. Jogini, M. P. Eastwood, R. O. Dror, D. E. Shaw, Principles of conduction and hydrophobic gating in K+ channels. *Proc. Natl. Acad. Sci. U.S.A.* **107**, 5833–5838 (2010).
46. P. P. Borbat, K. Surendhran, M. Bortolus, P. Zou, J. H. Freed, H. S. Mchaourab, Conformational motion of the ABC transporter MsbA induced by ATP hydrolysis. *PLoS Biol.* **5**, e271 (2007).
47. M. Yang, N. Livnat Levanon, B. Acar, B. Aykac Fas, G. Masrati, J. Rose, N. Ben-Tal, T. Haliloglu, Y. Zhao, O. Lewinson, Single-molecule probing of the conformational homogeneity of the ABC transporter BtuCD. *Nat. Chem. Biol.* **14**, 715–722 (2018).
48. B. Wiseman, A. Kilburg, V. Chaptal, G. C. Reyes-Mejia, J. Sarwan, P. Falson, J. M. Jault, Stubborn contaminants: Influence of detergents on the purity of the multidrug ABC transporter BmrA. *PLOS ONE* **9**, e114864 (2014).
49. E. Heftmann, S. T. Ko, R. D. Bennett, Response of steroids to sulfuric acid in thin-layer chromatography. *J. Chromatogr.* **21**, 490–494 (1966).
50. C. M. Hebling, C. R. Morgan, D. W. Stafford, J. W. Jorgenson, K. D. Rand, J. R. Engen, Conformational analysis of membrane proteins in phospholipid bilayer nanodiscs by hydrogen exchange mass spectrometry. *Anal. Chem.* **82**, 5415–5419 (2010).
51. A. M. Lau, J. Claesen, K. Hansen, A. Politis, Deuteros 2.0: Peptide-level significance testing of data from hydrogen deuterium exchange mass spectrometry. *Bioinformatics* **37**, 270–272 (2021).
52. Y. Perez-Riverol, A. Csordas, J. Bai, M. Bernal-Llinares, S. Hewapathirana, D. J. Kundu, A. Inuganti, J. Griss, G. Mayer, M. Eisenacher, E. Pérez, J. Uszkoreit, J. Pfeuffer, T. Sachsenberg, Ş. Yılmaz, S. Tiwary, J. Cox, E. Audain, M. Walzer, A. F. Jarnuczak, T. Ternent, A. Brazma, J. A. Vizcaíno, The PRIDE database and related tools and resources in 2019: Improving support for quantification data. *Nucleic Acids Res.* **47**, D442–D450 (2019).
53. J. Y. Lee, J. G. Yang, D. Zhitnitsky, O. Lewinson, D. C. Rees, Structural basis for heavy metal detoxification by an Atm1-type ABC exporter. *Science* **343**, 1133–1136 (2014).
54. L. Zimmermann, A. Stephens, S. Z. Nam, D. Rau, J. Kübler, M. Lozajic, F. Gabler, J. Söding, A. N. Lupas, V. Alva, A completely reimplemented MPI bioinformatics toolkit with a new HHpred server at its core. *J. Mol. Biol.* **430**, 2237–2243 (2018).
55. M. A. Lomize, I. D. Pogozheva, H. Joo, H. I. Mosberg, A. L. Lomize, OPM database and PPM web server: Resources for positioning of proteins in membranes. *Nucleic Acids Res.* **40**, D370–D376 (2012).
56. J. Lee, X. Cheng, J. M. Swails, M. S. Yeom, P. K. Eastman, J. A. Lemkul, S. Wei, J. Buckner, J. C. Jeong, Y. Qi, S. Jo, V. S. Pande, D. A. Case, C. L. Brooks III, A. D. MacKerell Jr., J. B. Klauda, W. Im, CHARMM-GUI input generator for NAMD, GROMACS, AMBER, OpenMM, and CHARMM/OpenMM simulations using the CHARMM36 additive force field. *J. Chem. Theory Comput.* **12**, 405–413 (2016).
57. B. Hess, C. Kutzner, D. van der Spoel, E. Lindahl, GROMACS 4: Algorithms for highly efficient, load-balanced, and scalable molecular simulation. *J. Chem. Theory Comput.* **4**, 435–447 (2008).
58. U. Essmann, L. Perera, M. L. Berkowitz, T. Darden, H. Lee, L. G. Pedersen, A smooth particle mesh Ewald method. *J. Chem. Phys.* **103**, 8577–8593 (1995).
59. S. Páll, B. Hess, A flexible algorithm for calculating pair interactions on SIMD architectures. *Comput. Phys. Commun.* **184**, 2641–2650 (2013).
60. G. Bussi, D. Donadio, M. Parrinello, Canonical sampling through velocity rescaling. *J. Chem. Phys.* **126**, 014101 (2007).
61. M. Parrinello, A. Rahman, Polymorphic transitions in single crystals: A new molecular dynamics method. *J. Appl. Phys.* **52**, 7182–7190 (1981).
62. K. Vanommeslaeghe, E. Hatcher, C. Acharya, S. Kundu, S. Zhong, J. Shim, E. Darian, O. Guvench, P. Lopes, I. Vorobyov, Mackerell AD Jr, CHARMM general force field: A force field for drug-like molecules compatible with the CHARMM all-atom additive biological force fields. *J. Comput. Chem.* **31**, 671–690 (2010).

Acknowledgments: We thank K. Martin Pos for the gift of the CD43(DE3)Δ*AcrB E. coli* strain and H. Krügel for those of *B. subtilis* 168 and 8R. We thank L. Martinez for input in the BrmA purification process in introducing the cholate-DDM mixture. We thank the Synchrotron SOLEIL and ESRF staff, the crystallogenesis platform from SFR Bioscience UMS 3444, and IBCP. We thank C. Von Rhein and P. Legrand for the help in anisotropic data processing. Cryo-EM sample screening, optimization, and data collection were performed at the Cryo-EM Swedish National Facility in Stockholm, Sweden, funded by the Knut and Alice Wallenberg, Family Erling Persson and Kempe Foundations, SciLifeLab, Stockholm University, and the Umeå University. B.W. thanks M. Carroni and J. Conrad from the Swedish National Facility in Stockholm for the technical assistance in cryo-EM data collection. We thank the staff of beamline CM01 at ESRF for rapid access data collection through the proposal MX2344. We also thank the reviewers for the constructive inputs that contributed to substantial improvement of the manuscript. Last but not least, P.F. thanks G. Deleage for the constant support along these years, particularly at the beginning of the study. **Funding:** This work was supported by the Centre National de la Recherche Scientifique (CNRS), l'Institut National de la Santé et de la Recherche Médicale (INSERM), the Lyon University, the Grenoble-Alpes University, the French Research Agency (ANR), and Auvergne-Rhône-Alpes region (ARC1) as follows: ARC1-CLAMP grant no. 13 009802 01 to A.B., V.C., and P.F.; ANR-CLAMP-13-BSV5-0001-01 to P.F., A.B., V.C., and A.K.; ANR-NMX-14-CE09-0024-03 to P.F., J.-M.J., and V.C.; ANR-CAVEOTANK-17-CE11-0015-03 to P.F. and V.C.; ANR-CLAMP2-18-CE11-0002-01 to P.F., A.B., M.H., and V.C.; ANR-17-EURE-0003 (CBH-EUR-GS) to A.B. and M.P.; and ANR-19-CE11-0023-01 to C.O., V.C., J.-M.J., and P.F. Molecular dynamics calculations were carried out at CINES, GENCI grant no.

A0040710138 to L.M. Financial support was also provided to M.H. by the Swedish Research Council (2017-04018) and the Knut and Alice Wallenberg Foundation (2017.0275). A.K. and V.Z. PhDs were funded by ARC1 and EDISS school, respectively. K.-A.N.'s PhD was funded by EDCSV of Grenoble-Alpes University. B.W.'s postdoc was funded by the ANR projects CAVEOTANK and CLAMP2. J.E. was funded by the ANR CLAMP2. The HDX-MS experiments were supported by the French Ministry of Research (Investissements d'Avenir Program, Proteomics French Infrastructure, ANR-10-INBS-08), the Fonds Européens de Développement Régional Toulouse Métropole, and the Région Midi-Pyrénées. The cryo-EM data for resolving the apo-BmrA structure were collected using the platforms of the Grenoble Instruct–ERIC Center (ISBG; UMS 3518 CNRS-CEA-UGA-EMBL) within the Grenoble Partnership for Structural Biology (PSB), supported by FRISBI (ANR-10-INBS-05-02) and GRAL, financed within the University Grenoble Alpes graduate school (Ecoles Universitaires de Recherche) CBH-EUR-GS (ANR-17-EURE-0003). The electron microscope facility is supported by the Auvergne-Rhône-Alpes Region, the Fondation pour la Recherche Médicale (FRM), the fonds FEDER, and the GIS–Infrastructures en Biologie Santé et Agronomie (IBiSA). **Author contributions:** V.C., V.Z., A.K., A.G., and S.M. purified BmrA and carried out the crystallogenesis experiments. M.H. granted access to cryo-EM equipment, and B.W. carried out the cryo-EM experiments for the R6G-BmrA complex. G.S., A.G., and V.C. carried out the cryo-EM experiments with the apo form using the Grenoble Instruct–ERIC platform. V.Z., V.C., and P.F. carried out the detergent quantifications. V.C., V.Z., A.G., and B.W. resolved the structures. C.O. and V.Z. prepared the E504A mutant. V.Z., C.O., S.M., and A.G. carried out the ATPase assays. A.B. and P.F. conceived the crystallization additives, and K.-A.N., M.P., and A.B. synthesized them. S.M. and P.F. carried out the thermostability assays. J.Mart., J.E., and L.M. carried out the dynamic simulations. W.J., M.D.C., and J.Marc. performed the HDX-MS experiments supervised by J.-M.J. and C.O. J.-M.J. and C.O. contributed to the analysis of the results. V.Z., A.G., M.D.C., S.M., C.O., J.-M.J., V.C., and P.F. carried out the biochemical experiments. P.F. managed the overall project. The manuscript was written through contributions of all the authors who gave their approval to its final version. **Competing interests:** P.F., J.D., A.B., M.P., K.-A.N., and S.M. are inventors on a patent related to this work filed by the Centre National de la Recherche Scientifique, the Claude Bernard–Lyon 1 University and the Grenoble–Alpes University (nos. FR3063730B1, US20210130385A1, and WO2018162806A1), filed 9 March 2017, published 13 September 2018 (WO2018162806A1), 6 May 2021 (US20210130385A1), and 17 September 2021 (FR3063730B1). Crystallization additive requests can be addressed for research only to pierre.falson@univ-lyon1.fr or to ahcene.boumendjel@univ-grenoble-alpes.fr. The other authors declare that they have no competing interests. **Data and materials availability:** Crystal and cryo-EM structures of BmrA-E504A [ATP-Mg^{2+}] have been deposited in the Protein Data Bank and Electron Microscopy Data Bank with the following codes: x-ray: PDB 6r72; cryo-EM (with R6G unresolved): PDB 6r81, EMDB 4749 (C2 symmetry); cryo-EM (with R6G resolved): PDB 7BG4, EMDB 12170 (no symmetry); cryo-EM (without R6G): PDB 7ow8, EMDB-13095. The HDX-MS data have been deposited to the ProteomeXchange Consortium via the PRIDE partner repository with the dataset identifier PXD027447. Simulations are available online on Zenodo, with the DOI 10.5281/zenodo.5543740. All data needed to evaluate the conclusions in the paper are present in the paper and/or the Supplementary Materials.

Submitted 4 February 2021
Accepted 30 November 2021
Published 26 January 2022
10.1126/sciadv.abg9215